Histidine-rich glycoprotein-induced vascular normalization improves EPR-mediated drug targeting to and into tumors

Benjamin Theek[a,b,1], Maike Baues[a,1], Felix Gremse[a], Robert Pola[c], Michal Pechar[c], Inka Negwer[d], Kaloian Koynov[d], Benjamin Weber[e], Matthias Barz[e], Willi Jahnen-Dechent[f], Gert Storm[b,g], Fabian Kiessling[a], Twan Lammers[a,b,g,*]

[a] Department of Nanomedicine and Theranostics, Institute for Experimental Molecular Imaging, RWTH Aachen University Clinic and Helmholtz Institute for Biomedical Engineering, Aachen, Germany
[b] Department of Targeted Therapeutics, Biomaterial Science and Technology, University of Twente, Enschede, The Netherlands
[c] Institute of Macromolecular Chemistry, Czech Academy of Science, Prague, Czech Republic
[d] Max Planck Institute for Polymer Research, Mainz, Germany
[e] Institute of Organic Chemistry, Johannes Gutenberg University, Mainz, Germany
[f] Biointerface Laboratory, RWTH Aachen University Clinic and Helmholtz Institute for Biomedical Engineering, Aachen, Germany
[g] Department of Pharmaceutics, Utrecht Institute for Pharmaceutical Sciences, Utrecht University, Utrecht, The Netherlands

ARTICLE INFO

ABSTRACT

Tumors are characterized by leaky blood vessels, and by an abnormal and heterogeneous vascular network. These pathophysiological characteristics contribute to the enhanced permeability and retention (EPR) effect, which is one of the key rationales for developing tumor-targeted drug delivery systems. Vessel abnormality and heterogeneity, however, which typically result from excessive pro-angiogenic signaling, can also hinder efficient drug delivery to and into tumors. Using histidine-rich glycoprotein (HRG) knockout and wild type mice, and HRG-overexpressing and normal t241 fibrosarcoma cells, we evaluated the effect of genetically induced and macrophage-mediated vascular normalization on the tumor accumulation and penetration of 10–20 nm-sized polymeric drug carriers based on poly(*N*-(2-hydroxypropyl)methacrylamide). Multimodal and multiscale optical imaging was employed to show that normalizing the tumor vasculature improves the accumulation of fluorophore-labeled polymers in tumors, and promotes their penetration out of tumor blood vessels deep into the interstitium.

1. Introduction

One of the biggest challenges in systemic anticancer drug therapy relates to the inefficient accumulation of intravenously (i.v.) administered chemotherapeutic agents at pathological sites. Classical chemotherapeutic drugs typically suffer from a short circulation half-life (as a result of rapid renal excretion), and from a large volume of distribution (resulting in systemic side effects) [1,2]. For several decades, scientists have been developing materials and methods to overcome these problems, primarily via the incorporation of low-molecular-weight chemotherapeutic agents in 1–100(0) nm-sized drug delivery systems. These carrier materials, which typically include polymers, micelles and liposomes, are larger than the renal clearance threshold, thus having a completely different biodistribution profile, and they accumulate more efficiently at pathological sites than free drug molecules [3–5].

In case of drug targeting to tumors, pathophysiological characteristics such as hypervascularity, hyperpermeability and impaired lymphatic drainage allow nanomedicines to accumulate more efficiently and more selectively at sites of malignancy, via the so-called enhanced permeability and retention (EPR) effect [6,7]. The EPR effect, however, is met with increasing scrutiny, and an increasing number of papers has questioned its presence, prominence and relevance [8–11]. One of the potential problems associated with leaky blood vessels, for instance, is the relatively high interstitial fluid pressure (IFP) which is typical for tumors [12,13]. Consequently, convective transport processes, in particular the penetration of drugs and drug delivery systems from the tumor blood vessels deep into the interstitium, are impaired.

Furthermore, the EPR effect is not omnipresent in all tumors, resulting in a very high degree of inter- and intraindividual heterogeneity in the "passive" accumulation of nanomedicine formulations in tumors [14,15].

To improve the accumulation and distribution of nanomedicines in tumors, and to eventually enhance their therapeutic efficacy, several pharmacological and physical vessel modulation strategies have been explored over the years [8,16]. In this context, a popular recent pharmacological strategy is vascular normalization, which aims to improve tumor-directed drug delivery via partially counteracting pro-angiogenic signaling in tumors [17–19]. Angiogenesis, i.e. the formation of new blood vessels from pre-existing ones, is a tightly controlled process under normal physiological conditions. However, during tumor development, proliferating cancer cells and hypoxia result in the overproduction of vascular growth factors, such as VEGF. Already in the 1970s, the importance of angiogenesis for the development of tumors was realized, and strategies to starve tumors to death by pharmacologically inhibiting angiogenesis were suggested [20]. While anti-angiogenic (anti-VEGF) monotherapies failed in the clinic, they presented with clear added value when combined with chemotherapy and/or radiotherapy [21–23]. This enhanced efficacy can be explained - at least in part - by a phenomenon termed vascular normalization, which helps to improve the delivery of drug molecules and oxygen to tumors [17,24–26].

The first vessels which respond to anti-angiogenic therapy are immature and leaky blood vessels. In a recent clinical study, Jain and colleagues showed that neoadjuvant bevacizumab (anti-VEGF antibody) treatment in HER2-negative breast cancer patients decreased the IFP and increased the fraction of pericyte-covered vessels, leading to a more normalized and better perfused vascular network, and to improved drug delivery [27]. Both standard chemotherapeutic drugs and metronomically administered anticancer agents have been shown to profit from vascular normalization [28], and also in case of

nanomedicines, vascular normalization has already been shown to be able to improve drug delivery and anti-tumor efficacy [29–31]. However, it seems to occur in a size-dependent manner, with the normalization-induced reduction in pore size hindering the extravasation of relatively large nanomedicines, such as 100 nm-sized Doxil® liposomes, while promoting the accumulation and efficacy of smaller sized nanomedicines, such as the ones obtained upon the i.v. administration of Abraxane®, which in the blood stream disintegrates into 10 nm-sized self-assemblies of paclitaxel and endogenous albumin [32].

Tumor-associated macrophages (TAM) play a key role in vascular normalization. TAM are typically polarized towards a more M2-like phenotype, which promotes angiogenesis and immunosuppression [33]. One of the first studies investigating the effect of vascular normalization mediated via the repolarisation of TAM, from an alternatively activated and pro-angiogenic M2-like phenotype towards a more classically activated and anti-angiogenic M1-like phenotype, focused on the histidine-rich glycoprotein (HRG) [34]. HRG is a highly abundant plasma protein which suppresses the expression of the pro-angiogenic placental growth factor (PlGF). PlGF is overexpressed in several tumor types and fuels angiogenesis by binding to VEGFR1 [35–37]. By inhibiting PlGF signaling, HRG expression protects against tumor growth and metastasis, via modulation of macrophage polarization and induction of vascular normalization [19,33,38,39].

We here used HRG-knockout and wild type mice, and HRG-overexpressing and normal t241 fibrosarcoma cells, to systematically study the effect of macrophage-mediated vascular normalization on the tumor accumulation and penetration of 10–20 nm-sized polymeric drug carriers based on poly(*N*-(2-hydroxypropyl)methacrylamide) (pHPMA). As exemplified by Fig. 1, we hypothesized that increased expression of HRG drives the polarization of TAM towards an anti-angiogenic M1-like phenotype, resulting in normalized tumor blood vessels, and in improved tumor-targeted drug delivery.
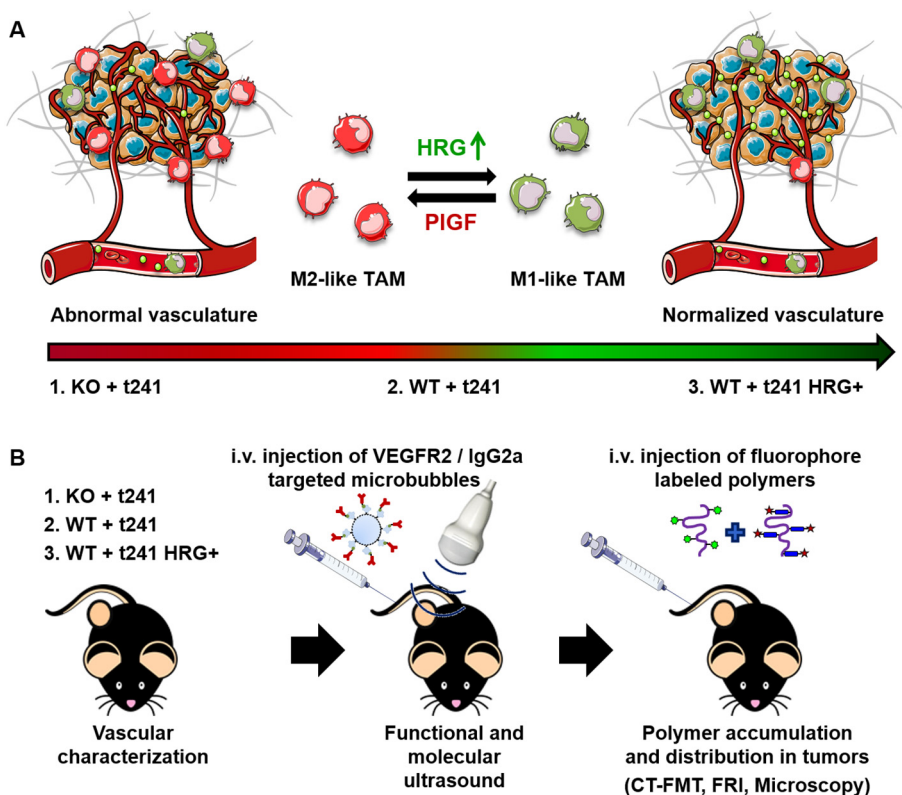

Fig. 1. Study design. (A) Expression of histidine-rich glycoprotein (HRG) affects the polarization of tumor-associated macrophages (TAM) and induces an M1-like anti-angiogenic (and vascular normalization) phenotype in tumors, via the downregulation of the placental growth factor (PlGF). (B) Three different genetic model systems were used to assess the impact of HRG knockout and (over-) expression on the accumulation and penetration of fluorophore-labeled 10–20 nm-sized polymeric drug carriers in t241 fibrosarcoma tumors. Knockout mice (KO) lacking HRG and wild type (WT) mice expressing HRG at physiological levels were implanted with t241 fibrosarcoma tumor cells. The latter mice were also implanted with t241 cells overexpressing HRG, to further promote local HRG-mediated vascular normalization. In these three mouse models, functional and molecular ultrasound, as well as multimodal and multiscale optical imaging, were employed to assess the effect of HRG-mediated vascular normalization on the accumulation and penetration of 10–20 nm-sized pHPMA-based polymeric drug delivery systems.

2. Materials & methods

2.1. Polymer synthesis

The synthesis of the pHPMA-based polymeric drug carriers was performed as described previously [40–42]. In short, a copolymer precursor was synthesized by radical copolymerization of (N-2-hydroxypropyl)methacrylamide (HPMA, 85 mol%) and 3-(N-methacryloyl glycylglycyl) thiazolidine-2-thione (Ma-GG-TT, 15 mol%) in DMSO at 50 °C for 6 h. Poly(HPMA-co-Ma-GG-TT) was dissolved in N,N'-dimethylacetamide and N,N'-diisopropylethylamine, together with the fluorophores ATTO 488-NH$_2$ and Dy750-NH$_2$. After a reaction time of 30 min, the polymer was aminolyzed with 1-aminopropan-2-ol, followed by precipitation using diethylether and centrifugation. Purification was performed using HPLC on Chromolith SemiPrep 100–10 mm and then by gel filtration on PD-10 desalting columns containing Sephadex G-25 resin in water (GE Healthcare, Solingen, Germany). Absorption measurements of the single fluorophore-labeled polymers were obtained with a spectrometer (Tecan Infinite 200 Pro; Tecan Trading AG, Männedorf, Switzerland). The molecular weight of the polymers was 67 kDa, polydispersity indices were 1.7, and the contents of ATTO 488 and Dy750 were 2.1% (w/w) and 1.6% (w/w). The hydrodynamic radius of the polymers was determined by dynamic light scattering (DLS) using a Nano-ZS instrument Zetasizer ZEN3600 (Malvern Panalytical Ltd., Malvern, United Kingdom).

2.2. Fluorescence correlation spectroscopy

Fluorescence correlation spectroscopy (FCS) experiments were performed, as previously described in [43], on a commercial setup LSM 880 (Carl Zeiss AG, Jena, Germany), with a Zeiss C-Apochromat 40×/ 1.2 W water immersion objective. The excitation was done by an Argon Laser (488 nm) or a TiSa laser (780 nm). For detection, an avalanche photodiode that enables single-photon counting was used. Eight-well polystyrene-chambered coverglass (Nunc™ Lab-Tek™, Thermo Fisher Scientific, Waltham, USA) was used as a sample cell. For each solution, a series of 10 measurements, with a total duration of 5 min, was performed at room temperature (23 °C). The obtained experimental autocorrelation curves were fitted with the following analytical model function:

$$G(t) = 1 + \left[1 + \frac{f_T}{1-f_T}e^{-t/\tau_T}\right]\frac{1}{N}\sum_{i=1}^{m}\frac{f_i}{\left[1 + \frac{t}{\tau_{Di}}\right]\sqrt{1 + \frac{t}{S^2\tau_{Di}}}} \tag{1}$$

here, N is the average number of diffusing fluorescence species in the observation volume, f_T and τ_T are the fraction and the decay time of the triplet state, τ_{Di} is the lateral diffusion time of the i-th species, f_i is the fraction of component i, and S is the so-called structure parameter, $S = z_0/r_0$, where z_0 and r_0 represent the axial and radial dimensions of the observation volume.

Furthermore, the lateral diffusion time, τ_{Di}, relates to the diffusion coefficient D_i through: [44].

$$\tau_{Di} = \frac{r_0^2}{4D_i} \tag{2}$$

The hydrodynamic radii R_H were calculated (assuming spherical polymeric nanomedicine formulations) using the Stokes-Einstein relation: $R_H = k_BT/6\pi\eta D$, where k_B is the Boltzmann constant, T is the temperature, and η is the viscosity of the solution. As the value of r_0 depends on the specific characteristics of the optical setup, a calibration was performed using reference standards with known diffusion coefficients, namely Alexa Fluor 488, $D = 4.35 \times 10^{-10}\,\mathrm{m^2/s}$ and IRDye® 800CW, $D = 2.45 \times 10^{-10}\,\mathrm{m^2/s}$ in water at 23 °C.

2.3. Animal experiments

All animal experiments were performed according to the regulations of the local and national ethical committee for animal welfare. C57BL/ 6 J mice (WT) were obtained from Charles River (Den Bosch, The Netherlands). B6-(HRG33)tm^{wja1} mice (KO), a viable and fertile HRG$^{-/}$ $^-$ null mutation have been described previously [45]. For both phenotypes, 5–8 week-old male and female mice were used. Group sizes ranged from 3 to 6. The mice were kept in individually ventilated cages with food and water ad-libitum as well as controlled light–dark cycles. One million t241 cells (i.e. murine fibrosarcoma) or HRG-overexpressing t241 cells (t241-HRG$^+$) [34] were inoculated subcutaneously into the right flank of the mice, and tumors were allowed to grow to 6–7 mm in diameter. Three days before the start of the drug delivery experiment, the diet was changed to chlorophyll-free food (ssniff Spezialdiäten GmbH, Soest, Germany), to reduce background fluorescence in the FMT analyses.

2.4. Contrast-enhanced ultrasound imaging

All in vivo ultrasound (US) experiments were conducted under continuous inhalation anesthesia, using 2% (vol/vol) isoflurane. The US device employed in this study was the VisualSonics Vevo2100 imaging system (Fujifilm Sonosite, Amsterdam, The Netherlands). During the examination, a heatable pad (Terra ComfortHeat Mat, Geilenkirchen, Germany) was used to avoid hypothermia of the animals. For the recording both linear and non-linear contrast mode were chosen with a transmission frequency of 21 MHz, power of 4% and 10 frames per second. To determine the VEGFR2 expression the monoclonal biotin anti-mouse CD309 antibody (BioLegend, San Diego, USA) was coupled to Vevo Micromarker® target-ready contrast agent (Fujifilm Sonosite, Amsterdam, The Netherlands) according to the manufacturer's instructions. Via a tail vein catheter, 1×10^8 microbubbles (MB) were injected and the inflow was simultaneously recorded to allow maximum intensity over time (MIOT) calculation. This procedure was repeated with an IgG2a-biotin control antibody (eBioscience, Frankfurt a.M., Germany). The signal increase after the injection of control microbubbles was used to calculate the relative blood volume. The signal difference before and after the high intensity burst was used to determine the relative amount of MB which bound to the target receptor, thereby providing information in the level of angiogenic marker expression.

2.5. Hybrid CT-FMT and FRI measurements

Hybrid computed tomography–fluorescence molecular tomography (CT-FMT) and fluorescence reflectance imaging (FRI) analyses were performed as described in [42,46,47]. Anesthetized mice were placed into a custom-made mouse bed enabling both CT (CT Imaging, Erlangen, Germany) and FMT (PerkinElmer, Waltham, USA) imaging. CT scans with 720 projections in 1.1 full rotations on a flat panel detector with the size of 1032×1012 pixels were obtained. Mice were then transferred to the FMT and FRI device, to assess the tumor accumulation and the biodistribution of the fluorescent polymers. For a partial body scan covering the tumor region, 45–60 FMT scan points lying on a grid with an inter-individual distance of 3 mm, were acquired from top and bottom orientation of each mouse. This procedure was performed directly, 4, 24 and 48 h after the i.v. injection of the polymers, in order to monitor the polymer accumulation longitudinally. After the last measurement, the mice were i.v. injected with rhodamine-lectin (to stain functional blood vessels and facilitate microscopy analyses) and sacrificed 10 min later. Tumors were excised and imaged ex vivo, in fluorescence reflectance mode at 750 nm, to obtain a high-resolution image of the polymer distribution in the tumor as a whole. Afterwards, they were embedded in a TissueTek O.C.T. (Sakura Finetek Europe, The Netherlands) mixture containing 1% (vol/vol) Imeron (Bracco,

Konstanz, Germany) and 5% (vol/vol) Intralipid (Fresenius Kabi, Pune, India) for ex vivo CT-FMT imaging and cryopreservation at −80 °C. One hundred μm-thick sections were freshly prepared from the frozen tumor samples and fluorescence reflectance images acquired, to monitor polymer distribution, using FRI and two-photon laser scanning microscopy (TPLSM).

2.6. Image analysis

The hybrid CT-FMT data sets were reconstructed, fused and analyzed using Imalytics Preclinical (Gremse-IT GmbH, Aachen, Germany). Tumor segmentation was based on the anatomical information obtained by CT. The FMT-based biodistribution data was loaded as an overlay, and the fluorescence signal allocated to the tumor was quantified and expressed as % of the injected dose (%ID) per 250 mm³ tumor (corresponding to the average volume of the tumors used in this study). In case of the FRI of 100 μm-thick sections the periphery was defined as a 5-pixel wide outer zone of the slice segmentation.

2.7. Two-photon laser scanning microscopy

Image stacks of 50 images with a step size of 1 μm were acquired using a 25× water-immersed objective mounted on the Olympus FV1000MPE multiphoton microscopy system and processed as described previously [48]. In each image stack, fluorescent polymers as well as perfused blood vessels (via rhodamine-lectin staining). TPLSM images were analyzed using the Imaris Software, Version 7.4 (Bitplane AG, Zurich, Switzerland). The micro-distribution of the ATTO488-containing fluorescent polymers, i.e. their extravasation from blood vessels into the tumor interstitium, was analyzed using a modified version of the "Dilate Surface" XTension in Imaris. For this purpose, initially, thresholding was applied on the basis of the rhodamine-lectin signal (to create a 3D vessel segmentation), and on the ATTO488 signal (to determine the volume of polymer distribution). The vessel segmentation was then automatically dilated, at step-sizes of 10 μm, 30 μm and 50 μm. Finally, the total amount of polymers detected within a 50 μm radius around the vessels was quantified by multiplying the relative polymer volume and the signal intensity. The relative micro-distribution of the polymers was calculated, by determining the relative amount of carrier material detected in each individual 3D segmentation, to compare the distribution of the polymers in tumors varying in HRG levels and vascular normalization status.

2.8. Immunofluorescence

Eight micrometer-thick tumor cryosections were fixed with 80% methanol (v/v) aqueous solution for 5 min and afterwards with −20 °C cold acetone for 2 min. Immunofluorescent stainings were performed with the following primary monoclonal antibodies: rabbit anti-mouse HRG antibody (The Scripps Research Institute, La Jolla, USA); rat anti-mouse CD31 (PECAM-1) antibody (BD Biosciences, Heidelberg, Germany); biotin anti-mouse smooth muscle actin (SMA) antibody (Progen Biotechnik, Heidelberg, Germany); rat anti-mouse F4-80 antibody (AbD Serotec, Puchheim, Germany); and rat anti-mouse CD206/Mrc-1 antibody (Acris Antibodies, Herford, Germany). Secondary antibodies were obtained from Dianova (Hamburg, Germany). DAPI (Sigma Aldrich, Taufkirchen, Germany) was used for nuclear counter-staining and sections were embedded with Mowiol® 4-88 (Roth, Karlsruhe, Germany). Images were acquired using the Axio Imager M2 microscopy system (Carl Zeiss AG, Jena, Germany).

2.9. Statistical analysis

Statistical analysis was performed using GraphPad Prism 5. All results are shown as average ± standard deviation. US and immuno-fluorescence analysis were performed using one-way ANOVA corrected

for multiple comparisons (Bonferroni). In vivo CT-FMT analysis on polymer accumulation and ex vivo measurements were evaluated as well with one-way ANOVA including the Bonferroni correction. For the polymer penetration analysis in TPLSM the two-way ANOVA with Bonferroni post-test was applied to investigate the interaction between the groups and the distance from the vessel surface. P-values of < 0.05 were considered to be statistically significant (*$p < 0.05$, **$p < 0.01$, ***$p < 0.001$).

3. Results & discussion

3.1. Polymer characterization

The DLS analysis of the non-fluorophore-modified pHPMA polymer revealed a hydrodynamic radius (R_H) of 4.1 nm and a polydispersity index of 1.7 (Sup. Fig. 1A). After coupling of Dy750 and Atto488, which have distinct absorption spectra (Sup. Fig. 1B) and optimal properties for in vivo CT-FMT imaging and ex vivo two-photon laser scanning microscopy, respectively, FCS experiments were performed to determine the R_H of the two fluorophore-labeled polymers. This was done in PBS and also in serum (Sup. Fig. 1C–D). The latter condition was included to evaluate the impact of serum protein adsorption (and protein corona formation) on the eventual size of the polymeric nanocarriers. After the coupling of the dyes to the polymer, an increase in size was observed. The Atto488-modified pHPMA polymer had a R_H of 6.3 nm in PBS and a size of 8.5 nm in plasma. When the polymer was labeled with Dy750, R_H values of 6.2 nm and 11.7 nm were found in PBS and plasma, respectively. These results demonstrate that the coupling of fluorophores to linear pHPMA polymers increases their apparent size, via the formation of less flexible unimolecular micelles and/or via promoting polymer-polymer-interactions. In addition, these findings indicate that the larger aromatic structures of near-infrared dyes (Dy750) more strongly induce the adsorption of plasma proteins as compared to standard fluorophores (Atto488). With an average hydrodynamic diameter of 10–20 nm, which typically ensures a prolonged circulation time (since the renal clearance threshold is 40–50 kDa; 7–8 nm), both fluorophore-modified pHPMA polymers were considered to be suitable model drug delivery systems for monitoring the effect of HRG-mediated vascular normalization on EPR-mediated tumor accumulation and tumor penetration.

3.2. Effect of HRG expression on the tumor vasculature

To systematically study the role of HRG-mediated vascular normalization on EPR-mediated tumor targeting, we first analyzed the HRG levels in the three tumor models, i.e. KO + t241, WT + t241 and WT + t241-HRG⁺. This was done via immunofluorescence stainings. Significant differences in HRG expression were found between the groups (Sup. Fig. 2). As expected, the KO + t241 and WT + t241 groups expressed significantly lower levels of HRG in tumors as compared to the WT + t241-HRG⁺ group. To investigate the effect of HRG-mediated normalization of the tumor vasculature, we applied contrast-enhanced functional (Fig. 2A–C) and molecular (Fig. 2D–F) ultrasound (US) imaging, as well as microscopy. For functional US, the maximum intensity over time (MIOT) image sequence was used, to determine the relative blood volume of tumors (Fig. 2A). Representative US images obtained at the beginning and at the end of MIOT analysis are shown in Fig. 2B. The images after contrast agent (i.e. microbubble; MB) injection exemplify the perfused regions within the tumors. Multiple perfused blood vessels could be identified in t241 tumors implanted in HRG-knockout and wild-type mice. In WT mice implanted with t241 cells overexpressing HRG, the relative blood vessel density was found to be lower than for the two other models, which hints towards pruning of highly angiogenic vessels. In line with this, when performing molecular US imaging using MB surface-modified with antibodies recognizing VEGFR2, we also observed lower angiogenic marker expression in t241
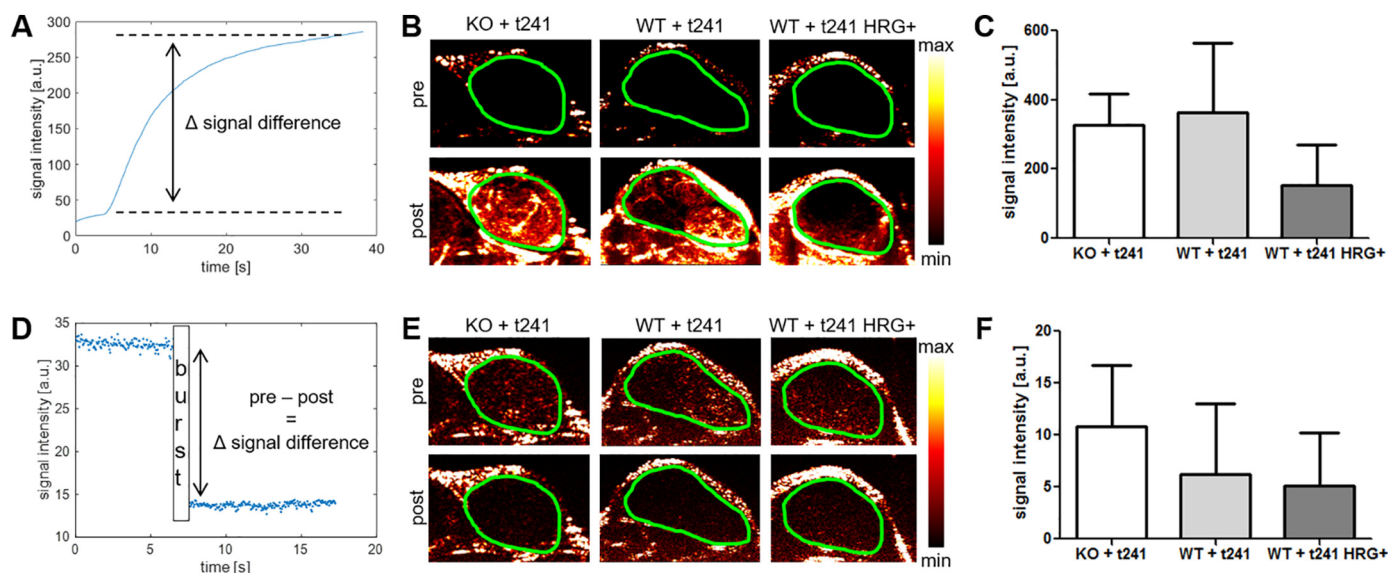
Fig. 2. Functional and molecular ultrasound (US) imaging to assess the effect of HRG expression on tumor vascularization and angiogenic marker expression. (A) An exemplary time-intensity curve of a maximum-intensity over time (MIOT) image sequence upon the i.v. injection of microbubbles (MB) as US contrast agents. MIOT analysis was used to determine the relative blood volume of tumors. (B–C) Representative MIOT images before and after MB injection (B) and the respective quantification of the signal differences (C) are shown for the three different mouse models. (D) To assess the expression of the angiogenic marker VEGFR2, MB surface-modified with anti-VEGFR2 antibodies were i.v. injected and allowed to bind to their target before they were destroyed using an US burst. (E-F) Imaging (E) and quantification (F) of the amount of VEGFR2-targeted MB which bound to tumor blood vessels in the three different models, indicating reduced levels of angiogenic marker expression in tumors with increased levels of HRG. Green circles indicate the tumors. Values represent average ± standard deviation of n = 3–6 tumors. (For interpretation of the references to colour in this figure legend, the reader is referred to the web version of this article.)

tumors overexpressing HRG. As exemplified by Fig. 2D, the signal difference before and after the destructive pulse is a relative measure for the number of MB bound to VEGFR2, and thus for the angiogenic status of the tumor vasculature. As hypothesized, t241 tumors grown in HRG-knockout mice (KO + t241) showed the highest signal difference and thus the highest expression of pro-angiogenic VEGFR2 on tumor blood vessels. They were followed by t241 tumors grown in WT mice (WT + t241), and the lowest number of VEGFR2-targeted MB were detected in HRG-overexpressing t241 tumors grown in WT mice (WT + t241-HRG$^+$) (Fig. 2E–F). This shows that the (over-) expression of HRG results in a lower blood vessel density and lower angiogenic potential of tumors.

To validate the in vivo US findings, we subsequently characterized the tumor vasculature via ex vivo immunohistochemistry and microscopy (Fig. 3). Staining of the endothelial cell marker CD31 (platelet-endothelial cell adhesion molecule 1; PECAM-1) showed that the average vessel density was significantly higher in t241 tumors grown in KO mice than in both t241 tumors grown in WT mice and in HRG-overexpressing t241 tumors grown in WT mice (P < 0.05; Fig. 3A,C). To investigate the functionality of tumors vessels, the relative fraction of lectin-positive vessels was determined. The lectin/CD31 positive fraction in the KO + t241 group was 46 ± 17% (Fig. 3D). In the WT + t241-HRG$^+$ group, this was found to be significantly higher (61 ± 21%; Fig. 3D). Tumors in the WT + t241 group had a lectin/CD31 positive fraction of 58 ± 18%. Since pericyte coverage is a key measure of vessel maturity, we also stained for α-smooth muscle actin (αSMA). In tumors grown in WT mice, we observed higher levels of αSMA than in mice lacking HRG, with the highest mean value observed in WT mice implanted with t241 overexpressing HRG (0.2 ± 0.1%; Fig. 3E). This tendency was also reflected in the vessel maturity score, in which the αSMA/CD31 positive fraction was substantially higher for the WT + t241-HRG$^+$ group (24 ± 18%) than for the KO + t241 group (15 ± 11%) (Fig. 3F).

As it is known that tumor-associated macrophages (TAM) play a key role in angiogenesis and HRG-mediated vascular normalization [49,50], we subsequently assessed the levels and the polarization status

of TAM. This was done via staining the pan-macrophage marker F4–80 and the macrophage mannose receptor-1 (Mrc-1), which is specifically expressed by pro-angiogenic M2-like macrophages. As shown in Fig. 3B and G, no significant differences in the overall amount of TAM were observed in the three different groups. In HRG-overexpressing t241 tumors grown in WT mice, however, a significantly lower fraction of Mrc-1-positive M2-like macrophages (52 ± 17%) was detected than in normal t241 tumors grown in HRG-knockout mice (65 ± 17%) (Fig. 3H). This is in line with findings reported in literature, showing that the overall amount of macrophages is not reduced, but only the M2-like macrophage population [34,38,39]. These studies showed that HRG expression contributes to the skewing of macrophages towards an anti-tumor M1-like phenotype. Importantly, it should be noted in this context that skewing TAM towards an M1 like-phenotype lead to a stronger growth delay compared to the complete depletion of all macrophages [34]. The importance of TAM polarization was also shown in a preclinical glioblastoma model. The reprogramming of TAM, from an M2-like to an M1-like phenotype, prolonged the survival of mice with glioblastoma, and is another piece of evidence for exploiting TAM plasticity to improve therapy outcome [51,52].

3.3. Effect of HRG-mediated vascular normalization on the tumor accumulation of polymers

To investigate how HRG-mediated vascular normalization influences the tumor accumulation of 67 kDa-sized HPMA copolymer-based drug delivery systems, hybrid CT-FMT imaging was performed (Fig. 4A). In line with the findings above on vascular normalization status, the highest polymer accumulation was found in the WT + t241-HRG$^+$ group, with 2.0 ± 0.6% of the injected dose (ID) per 250 mm^3 tumor at 48 h after the i.v. administration of the polymers (Fig. 4B). The second highest accumulation was found for the WT + t241 group, with 1.8 ± 1.1% ID per 250 mm^3. Polymer accumulation was least efficient in the most angiogenic tumor type, i.e. KO + t241, with 1.2 ± 0.2% ID per 250 mm^3 (Fig. 4B).

Next, the in vivo CT-FMT findings were validated ex vivo. As shown
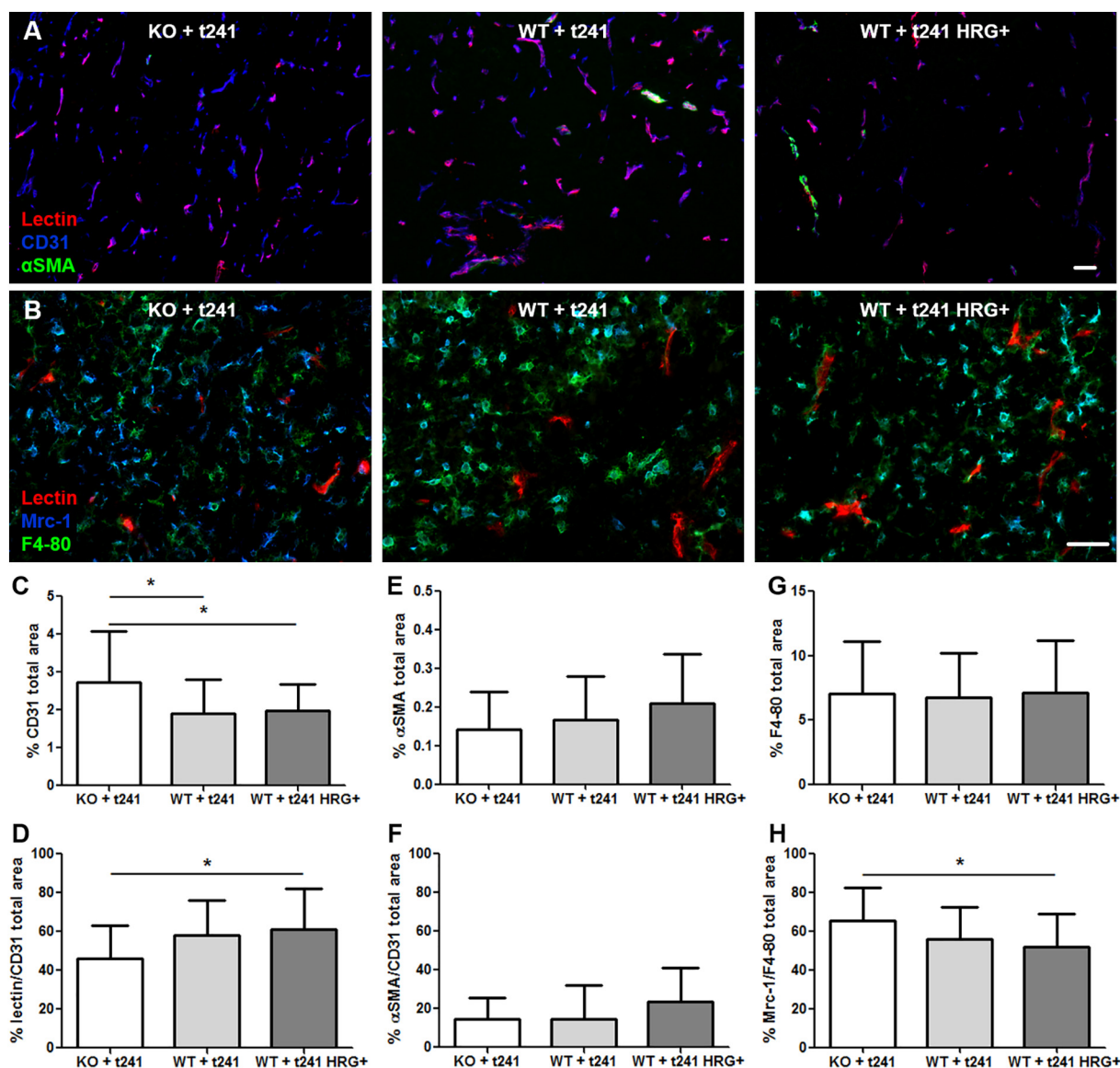
Fig. 3. Characterization of tumor blood vessels and tumor-associated macrophages in the three different mouse models. (A) Representative fluorescence microscopy images of the vasculature of t241 tumors in HRG-KO and WT mice, as well as in HRG-overexpressing t241 tumors in WT mice. Endothelial cells are stained with CD31 (blue), perfused blood vessels with rhodamine-lectin (red), and pericytes with αSMA (green). Scale bar: 50 μm. (B) Representative fluorescence microscopy images of lectin-stained perfused blood vessels (red), of all tumor-associated macrophages (TAM; via F4-80 [+] staining (green)) and of pro-angiogenic M2-like TAM (via Mrc-1 [+] staining (blue)). Scale bar: 50 μm. (C) The microvessel density, corresponding to the CD31 positive area fraction, is significantly lower in the presence of HRG. (D) Vessel functionality, depicted as % of rhodamine-lectin positive area/CD31 positive vessel area, increases with HRG presence. (E-F) Quantification of the pericyte marker αSMA shows a tendency towards more mature blood vessels in the presence of HRG. (G-H) F4-80 and Mrc-1 staining revealed similar amounts of TAM in the three groups (G), but a significantly higher ratio of Mrc-1 [+] pro-angiogenic M2-like TAM in tumors characterized by low levels of HRG (H). Values represent average ± standard deviation based on quantifying n = 4 sections in n = 3–6 tumors. * indicates $p < 0.05$. (For interpretation of the references to colour in this figure legend, the reader is referred to the web version of this article.)

in Fig. 4C–F, we were able to confirm that HRG-mediated vascular normalization positively affected polymer accumulation. To this end, tumors were excised, embedded in appropriate matrix material, and scanned ex vivo using both 3D-FMT and 2D-FRI, showing a significantly improved nanocarrier accumulation in tumors in the WT + t241-HRG [+] group. As compared to the KO + t241 group, values were up to 70% higher (P < 0.05). FRI was performed using 100 μm-thick tissue sections, differentiating between the peripheral zone (the outermost 5 pixels) and the remaining tumor core. Qualitative and quantitative assessment of these images shows that the polymers indeed accumulated better in the presence of HRG, and that this effect was strongest in the peripheral zone in HRG-overexpressing tumors (Fig. 4G–H). The observation that higher nanocarrier amounts were always detected in the

tumor periphery is in line with the literature, and likely results from the fact that the periphery typically contains larger and better perfused blood vessels (and a lower IFP) than the tumor core [53–56].

3.4. Effect of HRG-mediated vascular normalization on the tumor penetration of polymers

Besides macroscopically assessing tumor accumulation, we also analyzed the penetration of the polymeric drug carriers in tumors at the microscopic level. This was done using fluorescence and two-photon laser scanning microscopy (TPLSM) [57]. Homogenous and deep penetration of polymers out of the blood vessels into the tumor interstitium is highly important for efficient drug delivery and successful
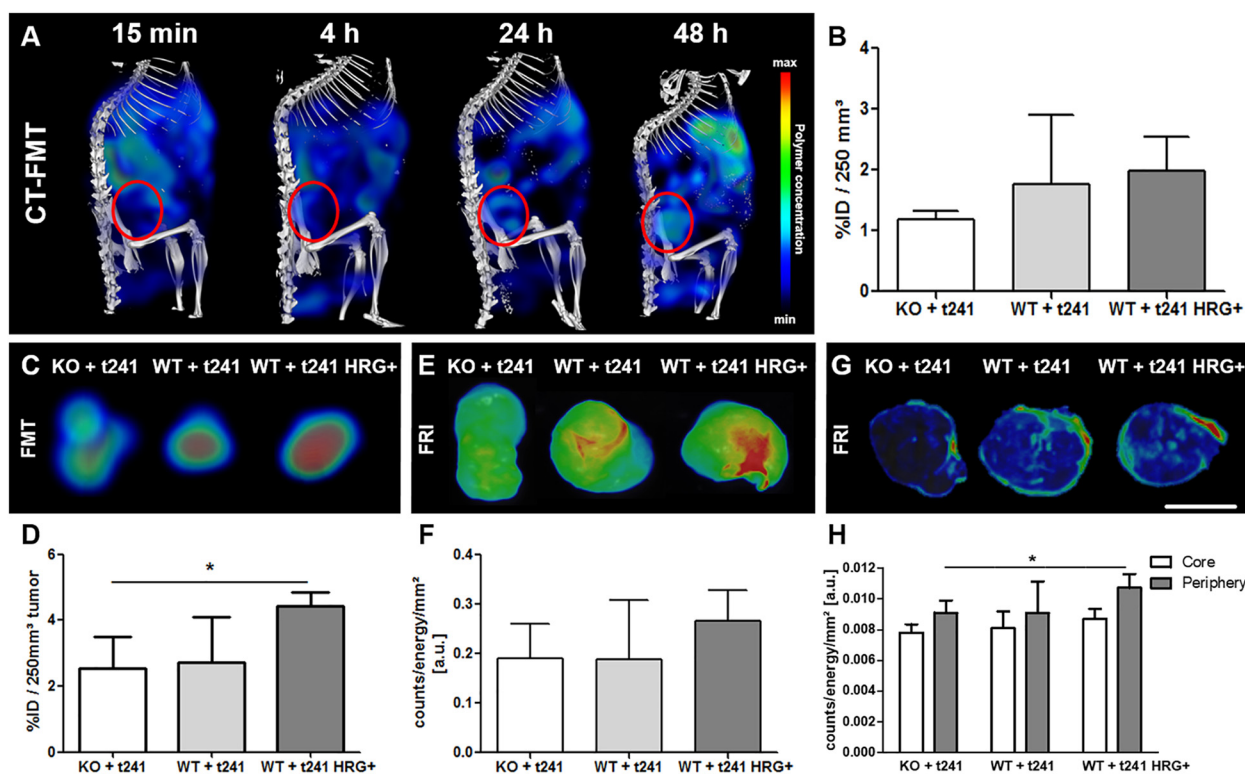
Fig. 4. In vivo and ex vivo optical imaging of the tumor accumulation of fluorophore-labeled polymers in the three tumor models. (A) Representative CT-FMT images of polymer accumulation in a WT + t241 mouse at several different time points after i.v. injection. The tumor region is encircled in red. (B) Quantification of the tumor accumulation of the polymeric drug carrier at 48 h post i.v. injection in KO and WT mice implanted with t241 tumors, and in WT mice implanted with HRG-overexpressing t241 tumors, demonstrating a tendency towards higher accumulation in tumors with normalized blood vessels. (C-F) Ex vivo FMT (C-D) and FRI (E-F) images and quantifications reveal a higher polymer accumulation in tumors expressing higher levels of HRG. (G-H) FRI analysis of 100 μm sections of tumors, demonstrating improved polymer accumulation particularly in the periphery of tumors expressing higher amounts of HRG. Values represent average ± standard deviation of n = 3–6 tumors. Scale bar: 5 mm. * indicates p < 0.05. (For interpretation of the references to colour in this figure legend, the reader is referred to the web version of this article.)

therapy [58]. Conversely, insufficient tumor penetration, not exceeding multiple cell layers beyond the blood vessel wall, is one of the most common pitfalls in tumor-targeted drug delivery [59,60]. To analyze polymer extravasation and penetration, the polymer-positive area percentages were determined at both 488 and 750 nm. Fig. 5A shows representative 2D images acquired with a standard fluorescence microscope. It was found that the more normalized the vasculature in the tumor was, the more polymers accumulated (Fig. 5C). Based on quantification at both 488 and 750 nm, the amount of polymers accumulating in tumors in the WT + t241-HRG$^+$ group (0.5% for 488 nm; 0.8% for 750 nm) was more than doubled in comparison to the KO + t241 group (0.2% for 488 nm; 0.3% for 750 nm).

We also visualized and quantified polymer penetration using TPLSM (Fig. 5B). This allowed us to assess, in a three-dimensional manner, the micro-distribution and penetration of polymers at distances of up to 50 μm around functional rhodamine-lectin-perfused tumor blood vessels. In line with the US and microscopy analyses in the three models, the perfused vessel volume decreased upon HRG-mediated vascular normalization (Fig. 5D). In spite of this, the amount of polymers accumulating in tumors with normalized blood vessels substantially increased (Fig. 5B). On top of this, and arguably even more importantly, the 3D-TPLSM analysis showed that HRG-mediated vascular normalization improved the ability of polymers to penetrate deeper into the tumor tissue (Fig. 5E). In the WT + t241 and WT + t241-HRG$^+$ groups, the relative polymer accumulation in tumor tissue located 30–50 μm away from the nearest blood vessel was more than twice as high than for the KO + t241 group. For the former two, the polymer-positive area fraction was 57 ± 15% (P < 0.001) and 61 ± 16% (P < 0.01), respectively, as compared to only 25 ± 21% for the latter. This finding

demonstrates that vascular normalization strongly potentiates the penetration and the micro-distribution of 10–20 nm-sized polymeric drug carriers in tumors.

Overall, we show that HRG-induced vascular normalization improves the delivery of prototypic polymeric drug carriers to and into tumors. Our vascular normalization strategy (i.e. genetically induced vs. pharmacologically mediated) is based on the skewing of TAM towards an anti-tumoral M1-like macrophage phenotype. The effect of HRG relies on the downregulation of PlGF, and its enhanced expression has been shown to play a key role in the inhibition of tumor growth and metastatic spread [34,38]. We used three different mouse models, with gradually increasing HRG levels in tumors, to analyze how normalized blood vessels affect polymer-based drug delivery to tumors at the macroscopic and microscopic level. Strategies to normalize the tumor vasculature are frequently discussed as an emerging concept to modulate the EPR effect [16,30,32,61,62]. However, finding the normalization window using antiangiogenic drug therapies is difficult, as these effects are highly dose- and time-dependent. Our genetic vascular normalization setup helps to overcome such limitations, and appears to be well suited for systematically studying the effect of vascular normalization on tumor accumulation of drugs and drug delivery systems.

Our findings are in line with the outcome of several clinical studies in which standard chemotherapeutic agents, metronomically administered anticancer drugs and radiotherapy have been shown to profit from vascular normalization [22,23,27,28]. In the future, neoadjuvant therapies which induce vascular normalization may also turn out to be useful for priming the tumor microenvironment for improved delivery and efficacy of targeted anticancer agents, including e.g. nanomedicinal drug formulations and immunomodulating antibodies [49,63,64].
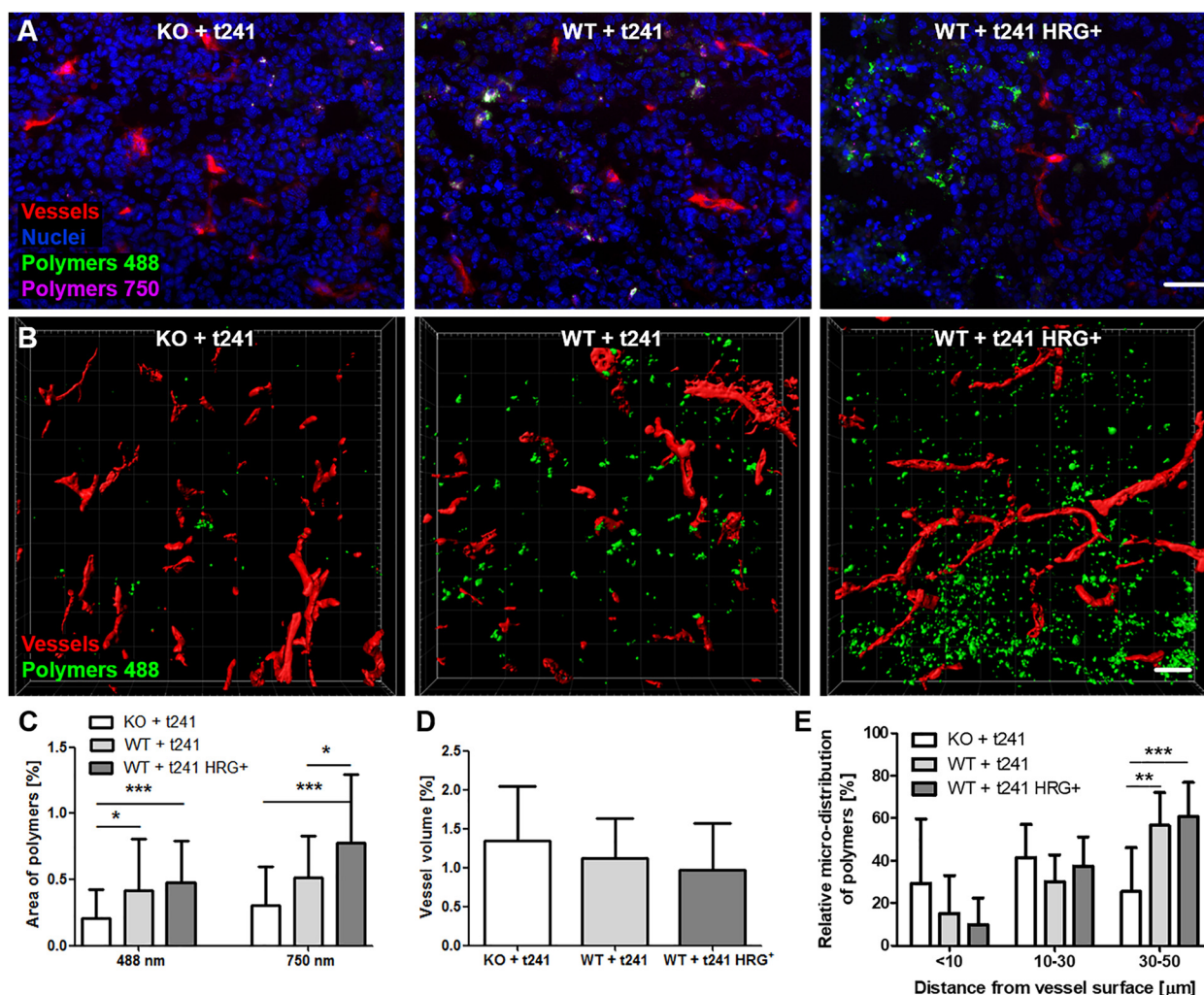
Fig. 5. Penetration of polymeric drug carriers in tumors with normalized blood vessels. (A) Exemplary immunofluorescence images showing the amount of blood vessels (red), cell nuclei (blue), ATTO 488-labeled (green) and Alexa-750-labeled (violet) polymers. Scale bar: 50 μm. (B) Surface-rendered two-photon laser scanning microscopy (TPLSM) image stacks with perfused blood vessels (red) and polymers (green). Scale bar: 50 μm. (C) A good correlation between the accumulation of polymers labeled with ATTO 488 and Alexa-750 is observed, in both cases indicating that polymer accumulation increases as a result of HRG-mediated vascular normalization. (D) TPLSM-based quantification indicates a somewhat lower blood volume upon HRG-mediated vascular normalization. (E) The penetration of polymers out of the blood vessels deep into the tumor interstitium significantly increases as a result of HRG-mediated vascular normalization. Values represent average ± standard deviation based on quantifying n = 3–4 sections in n = 3–6 different tumors. *$p < 0.05$, **$p < 0.01$, ***$p < 0.001$. (For interpretation of the references to colour in this figure legend, the reader is referred to the web version of this article.)

4. Conclusion

High heterogeneity in EPR-mediated tumor accumulation and poor penetration are among the key reasons explaining the relatively disappointing clinical performance of tumor-targeted nanomedicines. To reduce the high inter- and intraindividual heterogeneity in nanomedicine accumulation and penetration, several different EPR modulation strategies have been explored. Vascular normalization, which can be induced by anti-angiogenic agents, is a promising neoadjuvant therapy that may help to make the tumors more amenable to nanomedicine therapies. Using HRG-knockout mice and HRG-overexpressing cancer cells, we generated mouse tumors which contain a progressively normalized tumor vasculature, and we show that HRG-mediated vascular normalization improves the accumulation and the penetration of 10–20 nm-sized polymeric drug carriers. These findings indicate that priming tumor blood vessels and the microenvironment may help to improve the outcome of nanomedicine-based anticancer therapy.

Disclosure

overexpressing t241 and empty vector t241 fibrosarcoma cells were kindly provided by Prof. Lena Claesson-Welsh (Department of Immunology, Genetics and Pathology, Rudbeck Laboratory, Uppsala University). Image templates, provided by Servier Medical Art (http://smart.servier.com/), were employed for preparing the graphical abstract and Fig. 1.

Appendix A. Supplementary data

Supplementary data to this article can be found online at https://doi.org/10.1016/j.jconrel.2018.05.002.

References

[1] R. Langer, Drug delivery and targeting, Nature 392 (1998) 5–10.
[2] T.M. Allen, P.R. Cullis, Drug delivery systems: entering the mainstream, Science 303 (2004) 1818–1822.
[3] D. Peer, J.M. Karp, S. Hong, O.C. Farokhzad, R. Margalit, R. Langer, Nanocarriers as an emerging platform for cancer therapy, Nat. Nanotechnol. 2 (2007) 751–760.
[4] S. Nie, Understanding and overcoming major barriers in cancer nanomedicine, Nanomedicine (London) 5 (2010) 523–528.
[5] B. Theek, L.Y. Rizzo, J. Ehling, F. Kiessling, T. Lammers, The Theranostic path to personalized nanomedicine, Clin. Transl. Imaging 2 (2014) 66–76.
[6] H. Maeda, H. Nakamura, J. Fang, The EPR effect for macromolecular drug delivery to solid tumors: improvement of tumor uptake, lowering of systemic toxicity, and distinct tumor imaging in vivo, Adv. Drug Deliv. Rev. 65 (2013) 71–79.
[7] N. Bertrand, J. Wu, X. Xu, N. Kamaly, O.C. Farokhzad, Cancer nanotechnology: the impact of passive and active targeting in the era of modern cancer biology, Adv. Drug Deliv. Rev. 66 (2014) 2–25.
[8] F. Danhier, To exploit the tumor microenvironment: since the EPR effect fails in the clinic, what is the future of nanomedicine? J. Control. Release 244 ((2016) 108–121.
[9] S. Wilhelm, A.J. Tavares, Q. Dai, S. Ohta, Analysis of nanoparticle delivery to tumours, Nat. Rev. Mater. (2016) 1.
[10] T. Lammers, F. Kiessling, M. Ashford, W. Hennink, D. Crommelin, G. Storm, Cancer nanomedicine: is targeting our target? Nat Rev Mater. (2016) 1.
[11] U. Prabhakar, H. Maeda, R.K. Jain, E.M. Sevick-Muraca, W. Zamboni, O.C. Farokhzad, S.T. Barry, A. Gabizon, P. Grodzinski, D.C. Blakey, Challenges and key considerations for the enhanced permeability and retention effect for nanomedicine drug delivery in oncology, Cancer Res. 73 (2013) 2412–2417.
[12] M. Mohammadi, P. Chen, Effect of microvascular distribution and its density on interstitial fluid pressure in solid tumors: a computational model, Microvasc. Res. 101 (2015) 26–32.
[13] J. Zhao, H. Salmon, M. Sarntinoranont, Effect of heterogeneous vasculature on interstitial transport within a solid tumor, Microvasc. Res. 73 (2007) 224–236.
[14] J. Fang, H. Nakamura, H. Maeda, The EPR effect: unique features of tumor blood vessels for drug delivery, factors involved, and limitations and augmentation of the effect, Adv. Drug Deliv. Rev. 63 (2011) 136–151.
[15] J.L. Perry, K.G. Reuter, J.C. Luft, C.V. Pecot, W. Zamboni, J.M. DeSimone, Mediating passive tumor accumulation through particle size, tumor type, and location, Nano Lett. 17 (2017) 2879–2886.
[16] T. Ojha, V. Pathak, Y. Shi, W.E. Hennink, C.T.W. Moonen, G. Storm, F. Kiessling, T. Lammers, Pharmacological and physical vessel modulation strategies to improve EPR-mediated drug targeting to tumors, Adv. Drug Deliv. Rev. 119 (2017) 44–60.
[17] R.K. Jain, Normalization of tumor vasculature: an emerging concept in antiangiogenic therapy, Science 307 (2005) 58–62.
[18] P. Carmeliet, R.K. Jain, Principles and mechanisms of vessel normalization for cancer and other angiogenic diseases, Nat. Rev. Drug Discov. 10 (2011) 417–427.
[19] S. Goel, D.G. Duda, L. Xu, L.L. Munn, Y. Boucher, D. Fukumura, R.K. Jain, Normalization of the vasculature for treatment of cancer and other diseases, Physiol. Rev. 91 (2011) 1071–1121.
[20] J. Folkman, Tumor angiogenesis: therapeutic implications, N. Engl. J. Med. 285 (1971) 1182–1186.
[21] B. Sitohy, J.A. Nagy, H.F. Dvorak, Anti-VEGF/VEGFR therapy for cancer: reassessing the target, Cancer Res. 72 (2012) 1909–1914.
[22] C.G. Willett, S.V. Kozin, D.G. Duda, E. di Tomaso, K.R. Kozak, Y. Boucher, R.K. Jain, Combined vascular endothelial growth factor-targeted therapy and radiotherapy for rectal cancer: theory and clinical practice, Semin. Oncol. 33 (2006) S35–S40.
[23] R.K. Jain, D.G. Duda, J.W. Clark, J.S. Loeffler, Lessons from phase III clinical trials on anti-VEGF therapy for cancer, Nat. Clin. Pract. Oncol. 3 (2006) 24–40.
[24] S. Goel, A.H. Wong, R.K. Jain, Vascular normalization as a therapeutic strategy for malignant and nonmalignant disease, Cold Spring Harb. Perspect. Med. 2 (2012) a006486.
[25] R.K. Jain, Normalizing tumor microenvironment to treat cancer: bench to bedside to biomarkers, J. Clin. Oncol. 31 (2013) 2205–2218.
[26] K. De Bock, S. Cauwenberghs, P. Carmeliet, Vessel abnormalization: another hallmark of cancer? Molecular mechanisms and therapeutic implications, Curr. Opin. Genet. Dev. 21 (2011) 73–79.
[27] S.M. Tolaney, Y. Boucher, D.G. Duda, J.D. Martin, G. Seano, M. Ancukiewicz, W.T. Barry, S. Goel, J. Lahdenrata, S.J. Isakoff, E.D. Yeh, S.R. Jain, M. Golshan, J. Brock, M. Snuderl, E.P. Winer, I.E. Krop, R.K. Jain, Role of vascular density and normalization in response to neoadjuvant bevacizumab and chemotherapy in breast cancer patients, Proc. Natl. Acad. Sci. U. S. A. 112 (2015) 14325–14330.
[28] F. Mpekris, J.W. Baish, T. Stylianopoulos, R.K. Jain, Role of vascular normalization in benefit from metronomic chemotherapy, Proc. Natl. Acad. Sci. U. S. A. 114 (2017) 1994–1999.
[29] I.A. Khawar, J.H. Kim, H.J. Kuh, Improving drug delivery to solid tumors: priming the tumor microenvironment, J. Control. Release 201 (2015) 78–89.
[30] R.K. Jain, T. Stylianopoulos, Delivering nanomedicine to solid tumors, Nat. Rev. Clin. Oncol. 7 (2010) 653–664.
[31] V.P. Chauhan, R.K. Jain, Strategies for advancing cancer nanomedicine, Nat. Mater. 12 (2013) 958–962.
[32] V.P. Chauhan, T. Stylianopoulos, J.D. Martin, Z. Popovic, O. Chen, W.S. Kamoun, M.G. Bawendi, D. Fukumura, R.K. Jain, Normalization of tumour blood vessels improves the delivery of nanomedicines in a size-dependent manner, Nat. Nanotechnol. 7 (2012) 383–388.
[33] Y. Huang, M. Snuderl, R.K. Jain, Polarization of tumor-associated macrophages: a novel strategy for vascular normalization and antitumor immunity, Cancer Cell 19 (2011) 1–2.
[34] C. Rolny, M. Mazzone, S. Tugues, D. Laoui, I. Johansson, C. Coulon, M.L. Squadrito, I. Segura, X. Li, E. Knevels, S. Costa, S. Vinckier, T. Dresselaer, P. Akerud, M. De Mol, H. Salomaki, M. Phillipson, S. Wyns, E. Larsson, I. Buysschaert, J. Botling, U. Himmelreich, J.A. Van Ginderachter, M. De Palma, M. Dewerchin, L. Claesson-Welsh, P. Carmeliet, HRG inhibits tumor growth and metastasis by inducing macrophage polarization and vessel normalization through downregulation of PlGF, Cancer Cell 19 (2011) 31–44.
[35] C. Fischer, M. Mazzone, B. Jonckx, P. Carmeliet, FLT1 and its ligands VEGFB and PlGF: drug targets for anti-angiogenic therapy? Nat. Rev. Cancer 8 (2008) 942–956.
[36] I.K. Poon, K.K. Patel, D.S. Davis, C.R. Parish, M.D. Hulett, Histidine-rich glycoprotein: the Swiss Army knife of mammalian plasma, Blood 117 (2011) 2093–2101.
[37] A.K. Olsson, H. Larsson, J. Dixelius, I. Johansson, C. Lee, C. Oellig, I. Bjork, L. Claesson-Welsh, A fragment of histidine-rich glycoprotein is a potent inhibitor of tumor vascularization, Cancer Res. 64 (2004) 599–605.
[38] S. Tugues, S. Honjo, C. Konig, O. Noguer, M. Hedlund, J. Botling, S. Deschoemaeker, M. Wenes, C. Rolny, W. Jahnen-Dechent, M. Mazzone, L. Claesson-Welsh, Genetic deficiency in plasma protein HRG enhances tumor growth and metastasis by exacerbating immune escape and vessel abnormalization, Cancer Res. 72 (2012) 1953–1963.
[39] A.L. Jones, M.D. Hulett, C.R. Parish, Histidine-rich glycoprotein: a novel adaptor protein in plasma that modulates the immune, vascular and coagulation systems, Immunol. Cell Biol. 83 (2005) 106–118.
[40] B. Rihova, M. Jelinkova, J. Strohalm, V. Subr, D. Plocova, O. Hovorka, M. Novak, D. Plundrova, Y. Germano, K. Ulbrich, Polymeric drugs based on conjugates of synthetic and natural macromolecules. II. Anti-cancer activity of antibody or (Fab')(2)-targeted conjugates and combined therapy with immunomodulators, J. Control. Release 64 (2000) 241–261.
[41] T. Etrych, T. Mrkvan, B. Rihova, K. Ulbrich, Star-shaped immunoglobulin-containing HPMA-based conjugates with doxorubicin for cancer therapy, J. Control. Release 122 (2007) 31–38.
[42] S. Kunjachan, F. Gremse, B. Theek, P. Koczera, R. Pola, M. Pechar, T. Etrych, K. Ulbrich, G. Storm, F. Kiessling, T. Lammers, Noninvasive optical imaging of nanomedicine biodistribution, ACS Nano 7 (2013) 252–262.
[43] D. Schaeffel, S. Yordanov, R.H. Staff, A. Kreyes, Y. Zhao, M. Schmidt, K. Landfester, J. Hofkens, H.J. Butt, D. Crespy, K. Koynov, Fluorescence correlation spectroscopy in dilute polymer solutions: effects of molar mass dispersity and the type of fluorescent labeling, ACS Macro Lett. 4 (2015) 171–176.
[44] R. Rigler, E. Elson, Fluorescence Correlation Spectroscopy: Theory and Applications, Springer, Berlin; New York, 2001.
[45] N. Tsuchida-Straeten, S. Ensslen, C. Schafer, M. Woltje, B. Denecke, M. Moser, S. Graber, S. Wakabayashi, T. Koide, W. Jahnen-Dechent, Enhanced blood coagulation and fibrinolysis in mice lacking histidine-rich glycoprotein (HRG), J. Thromb. Haemost. 3 (2005) 865–872.
[46] F. Gremse, D. Doleschel, S. Zafarnia, A. Babler, W. Jahnen-Dechent, T. Lammers, W. Lederle, F. Kiessling, Hybrid µCT-FMT imaging and image analysis, J. Vis. Exp. 100 (2015) e52770.
[47] F. Gremse, M. Stark, J. Ehling, J.R. Menzel, T. Lammers, F. Kiessling, Imalytics preclinical: interactive analysis of biomedical volume data, Theranostics 6 (2016) 328–341.
[48] B. Theek, M. Baues, T. Ojha, D. Mockel, S.K. Veettil, J. Steitz, L. van Bloois, G. Storm, F. Kiessling, T. Lammers, Sonoporation enhances liposome accumulation and penetration in tumors with low EPR, J. Control. Release 231 (2016) 77–85.
[49] Y. Huang, S. Goel, D.G. Duda, D. Fukumura, R.K. Jain, Vascular normalization as an emerging strategy to enhance cancer immunotherapy, Cancer Res. 73 (2013) 2943–2948.
[50] M. Jarosz-Biej, N. Kaminska, S. Matuszczak, T. Cichon, J. Pamula-Pilat, J. Czapla, R. Smolarczyk, D. Skwarzynska, K. Kulik, S. Szala, M1-like macrophages change tumor blood vessels and microenvironment in murine melanoma, PLoS ONE 13 (2018) e0191012.
[51] T.E. Peterson, N.D. Kirkpatrick, Y. Huang, C.T. Farrar, K.A. Marijt, J. Kloepper, M. Datta, Z. Amoozgar, G. Seano, K. Jung, W.S. Kamoun, T. Vardam, M. Snuderl, J. Goveia, S. Chatterjee, A. Batista, A. Muzikansky, C.C. Leow, L. Xu, T.T. Batchelor, D.G. Duda, D. Fukumura, R.K. Jain, Dual inhibition of Ang-2 and VEGF receptors normalizes tumor vasculature and prolongs survival in glioblastoma by altering macrophages, Proc. Natl. Acad. Sci. U. S. A. 113 (2016) 4470–4475.
[52] J. Kloepper, L. Riedemann, Z. Amoozgar, G. Seano, K. Susek, V. Yu, N. Dalvie, R.L. Amelung, M. Datta, J.W. Song, V. Askoxylakis, J.W. Taylor, C. Lu-Emerson, A. Batista, N.D. Kirkpatrick, K. Jung, M. Snuderl, A. Muzikansky, K.G. Stubenrauch,

O. Krieter, H. Wakimoto, L. Xu, L.L. Munn, D.G. Duda, D. Fukumura, T.T. Batchelor, R.K. Jain, Ang-2/VEGF bispecific antibody reprograms macrophages and resident microglia to anti-tumor phenotype and prolongs glioblastoma survival, Proc. Natl. Acad. Sci. U. S. A. 113 (2016) 4476–4481.

[53] S. Stapleton, M. Milosevic, I.F. Tannock, C. Allen, D.A. Jaffray, The intra-tumoral relationship between microcirculation, interstitial fluid pressure and liposome accumulation, J. Control. Release 211 (2015) 163–170.

[54] L. Li, J. Sun, Z. He, Deep penetration of nanoparticulate drug delivery systems into tumors: challenges and solutions, Curr. Med. Chem. 20 (2013) 2881–2891.

[55] H. Chen, W. Zhang, G. Zhu, J. Xie, X. Chen, Rethinking cancer nanotheranostics, Nat. Rev. Mater. 2 (2017).

[56] T. Stylianopoulos, R.K. Jain, Combining two strategies to improve perfusion and drug delivery in solid tumors, Proc. Natl. Acad. Sci. U. S. A. 110 (2013) 18632–18637.

[57] Q. Sun, T. Ojha, F. Kiessling, T. Lammers, Y. Shi, Enhancing tumor penetration of nanomedicines, Biomacromolecules 18 (2017) 1449–1459.

[58] H. Cabral, Y. Matsumoto, K. Mizuno, Q. Chen, M. Murakami, M. Kimura, Y. Terada, M.R. Kano, K. Miyazono, M. Uesaka, N. Nishiyama, K. Kataoka, Accumulation of sub-100 nm polymeric micelles in poorly permeable tumours depends on size, Nat. Nanotechnol. 6 (2011) 815–823.

[59] Z. Popovic, W. Liu, V.P. Chauhan, J. Lee, C. Wong, A.B. Greytak, N. Insin, D.G. Nocera, D. Fukumura, R.K. Jain, M.G. Bawendi, A nanoparticle size series for in vivo fluorescence imaging, Angew. Chem. Int. Ed. Eng. 49 (2010) 8649–8652.

[60] M.R. Dreher, W. Liu, C.R. Michelich, M.W. Dewhirst, F. Yuan, A. Chilkoti, Tumor vascular permeability, accumulation, and penetration of macromolecular drug carriers, J. Natl. Cancer Inst. 98 (2006) 335–344.

[61] H. Kobayashi, R. Watanabe, P.L. Choyke, Improving conventional enhanced permeability and retention (EPR) effects; what is the appropriate target? Theranostics 4 (2013) 81–89.

[62] P. Carmeliet, R.K. Jain, Molecular mechanisms and clinical applications of angiogenesis, Nature 473 (2011) 298–307.

[63] Q. Chen, L. Xu, J. Chen, Z. Yang, C. Liang, Y. Yang, Z. Liu, Tumor vasculature normalization by orally fed erlotinib to modulate the tumor microenvironment for enhanced cancer nanomedicine and immunotherapy, Biomaterials 148 (2017) 69–80.

[64] R.R. Ramjiawan, A.W. Griffioen, D.G. Duda, Anti-angiogenesis for cancer revisited: is there a role for combinations with immunotherapy? Angiogenesis 20 (2017) 185–204.